Battery Energy

WILEY

RESEARCH ARTICLE OPEN ACCESS

Multi-Phase Synergy Enhances Lithium-Ion Storage Performance of Transition Metal Oxalates

Liying Xue[1,2] | Stefanie Arnold[2] | Jean Gustavo de Andrade Ruthes[1,2] | Oliver Janka[3] | Chaochao Dun[4] | Volker Presser[1,2,5]

[1]INM - Leibniz Institute for New Materials, Saarbrücken, Germany | [2]Department of Materials Science & Engineering, Saarland University, Saarbrücken, Germany | [3]Inorganic Solid State Chemistry, Saarland University, Saarbrücken, Germany | [4]The Molecular Foundry, Lawrence Berkeley National Laboratory, Berkeley, USA | [5]saarene - Saarland Center for Energy Materials and Sustainability, Saarbrücken, Germany

Correspondence: Volker Presser (volker.presser@leibniz-inm.de)

Received: 30 November 2025 | **Revised:** 13 February 2026 | **Accepted:** 24 February 2026

Funding: State Chancellery Saarland, Grant/Award Number: EnFoSaar; China Scholarship Council, Grant/Award Number: 501100004543; Deutsche Forschungsgemeinschaft, Grant/Award Number: 501100001659; Office of Science, Grant/Award Number: 100006132

Keywords: anode materials | lithium-ion batteries | multi-phase structure | transition metal oxalates

ABSTRACT

Transition metal oxalates have been proven to be a promising electrode material for lithium-ion batteries. Here, we have designed a series of multi-phase transition metal oxalates with different structures and compositions by simply adjusting the proportions of five transition metal elements. Among them, the multi-phase mixture ($MC_2O_4{\cdot}2H_2O$ - CuC_2O_4 - $MC_2O_4{\cdot}2H_2O$, M = Mn, Fe, Co, Ni, Cu) provides a more stable framework for the material during lithiation and delithiation, effectively alleviating the structural collapse during the cycling process. In addition, the electron transport and fast charge compensation processes of multiple electrochemically active metal pairs also contribute to the improvement of performance. Therefore, the multi-phase transition metal oxalate TMOx-2 electrode with an additional CuC_2O_4 phase exhibits high reversible capacity and long-term cycling stability. After 400 cycles at 100 and 500 mA/g, the specific discharge capacities are 827 mAh/g and 498 mAh/g, respectively. Constructing multi-metal, multi-phase systems by combining different transition metals enables control over potential, reaction pathways, and stability of high-performance electrodes.

1 | Introduction

Lithium-ion batteries (LIBs), as highly efficient and rechargeable energy storage devices, have important applications in fields such as portable electronic devices and electric vehicles, and are one of the key technologies for achieving clean energy utilization [1]. Compared to other energy storage systems, LIBs have the advantages of high energy density, long cycle life, and a relatively low self-discharge rate [2–4]. Although cost and safety performance still need to be optimized, LIBs remain one of the best overall energy storage solutions [3].

Electrode materials limit (or enable) key performance metrics of LIBs, such as energy density, cycle life, and safety; therefore, optimizing the structure and composition of electrode materials is a primary way to improve battery performance [5, 6]. Transition metal oxalates (TMOx) provide wide availability at low cost [7, 8]. Compared to the low theoretical capacity of graphite (372 mAh/g) [9] and the severe volume expansion of silicon-based materials (~300%) [10], TMOx can achieve higher specific capacity through rapid redox reactions on or near the surface of up to 700–900 mAh/g [11]. Various transition metal oxalates, such as FeC_2O_4 [12], MnC_2O_4 [13], and CoC_2O_4 [14], have been used as anode materials and exhibited high capacities. Nevertheless, their large-scale application is still limited by the capacity decay caused by irreversible structural transitions, structural collapse [15], and electrode pulverization [16] during long-term cycling, which results in a disconnection between the active materials and the conductive networks.

https://doi.org/10.1002/bte2.70103

One strategy to enhance the lithium-ion storage capacity is the use of element substitution [17]. Due to the immobilization of M^{2+} (M stands for transition metal elements) and $C_2O_4{}^{2-}$ ions within the structure, MC_2O_4 generally exhibits poor electrical conductivity and often behaves as an insulator or a semiconductor with very low electrical conductivity [18]. However, their electrochemical properties can be modulated by introducing defects, substitution of other metal ions, constructing nanostructures, and synergistic interactions between different metal species can provide more Faraday active sites and increase their electrical conductivity [19]. Wang et al. used the CoC_2O_4 structure as the basic framework. They made full use of the alternating arrangement of bimetallic ions (Ni and Co) in the material to prepare a $Ni_{0.55}Co_{0.45}C_2O_4$ solid solution, which showed a higher specific capacity than that of single-metal oxalates [20]. León et al. prepared a series of two mixed transition metal oxalates (Co-Mn and Fe-Mn) using the reverse micellar method. The manganese cobalt oxalate with the best electrochemical performance still maintained a specific capacity of about 600 mAh/g after 75 cycles at a rate of 2 C [21]. Wei et al. employed a simple one-pot solvothermal method to prepare $Co_{0.52}Mn_{0.48}C_2O_4$, which demonstrated robust cycling performance with a specific discharge capacity of up to 1000 mAh/g after 100 cycles at a rate of 1 C [22].

New strategies for forming composite structured electrode materials by introducing structural units have emerged to improve electrochemical properties and endow the electrode materials with structural stability, attracting wide interest [23]. The use of bi-phase or multi-phase electrodes yields more active sites and concurrent good ionic conductivity [24]. For example, Wang et al. prepared a multi-phase metal sulfide (Bi_2S_3@C@CoS_2) with a hierarchical structure. Compared with the reported metal sulfides, the multi-phase structure has comparable or even better rate performance [25]. Liu et al. constructed a triple-conducting hybrid electrode consisting of the cubic phase $Ba_{0.5}Sr_{0.5}Co_{0.8}Fe_{0.2}O_{3\text{-}\delta}$ and the hexagonal phase $Ba_4Sr_4(Co_{0.8}Fe_{0.2})_4O_{16\text{-}\delta}$ by a stoichiometric tuning strategy, and the hybrid electrode with a two-phase synergistic effect exhibited promising electrochemical performance [26]. Zhang et al. obtained $FeC_2O_4 \cdot 2H_2O$ with two different crystal structures (monoclinic α-$FeC_2O_4 \cdot 2H_2O$ and orthorhombic β-$FeC_2O_4 \cdot 2H_2O$) by changing the solvothermal temperature. Compared to the single-phase samples, the multi-phase $FeC_2O_4 \cdot 2H_2O$ is more stable and has a shorter diffusion path [12]. The presence of two or more different components allows the properties of nanomaterials to be flexibly adjusted [27].

In this work, we report a series of novel TMOx-based hybrid electrodes with different crystal structures and compositions by controlling the content ratios of five transition metal elements in the raw materials. Electrochemical testing and characterization revealed that the TMOx-2 sample, which contains a separate copper oxalate phase, exhibited the best lithium-ion storage performance, with a discharge specific capacity of 827 mAh/g even after 400 cycles at a rate of 100 mA/g. This is due to the synergistic effect between CuC_2O_4 and two different polymorphs of $MC_2O_4 \cdot 2H_2O$. Furthermore, the electron transport and fast charge compensation processes of multiple electrochemically active metal pairs jointly contribute to the performance improvement. This composite structure will open new research directions for high-energy-density LIBs.

2 | Experiment

2.1 | Materials Synthesis

A series of multi-transition metal oxalates was synthesized by a simple co-precipitation method. Equimolar amounts of manganese chloride tetrahydrate ($MnCl_2 \cdot 4H_2O$, Sigma-Aldrich, ReagentPlus, 98.0%), ferrous chloride tetrahydrate ($FeCl_2 \cdot 4H_2O$, Sigma-Aldrich, ReagentPlus ≥ 99%), cobalt chloride hexahydrate ($CoCl_2 \cdot 6H_2O$, Sigma-Aldrich, ≥ 97%), nickel chloride hexahydrate ($NiCl_2 \cdot 6H_2O$, Sigma-Aldrich, ReagentPlus, 99.0%), and copper chloride dihydrate ($CuCl_2 \cdot 2H_2O$, Sigma-Aldrich, ACS reagent, ≥ 99.0%) were dissolved in Milli-Q water (less than 0.056 $\mu S\, cm^{-1}$ at 25°C) to prepare a solution with a transition metal ion concentration of 0.05 M, which is subsequently called solution A. Then, oxalic acid dihydrate ($H_2C_2O_4 \cdot 2H_2O$, Sigma-Aldrich, ACS reagent, ≥ 99%) was dissolved in Milli-Q water to prepare a 0.05 M equimolar oxalate solution, which is called solution B. Solution B was then slowly poured into solution A under magnetic stirring, and stirring was continued at room temperature for 4 h. After that, the mixture was filtered and washed several times, and the obtained products were dried at 60°C overnight to obtain TMOx-0. To obtain different compositions, the element ratio in solution A was adjusted, and the remaining steps followed a similar procedure. In other samples, the molar ratios of the elements in solution A are TMOx-1 (Mn: Fe: Co: Ni: Cu = 2: 4: 1: 1: 1), TMOx-2 (Mn: Fe: Co: Ni: Cu = 4: 2: 1: 1: 2), and TMOx-3 (Mn: Fe: Co: Ni: Cu = 4: 2: 1: 1: 4). Similarly, we prepared single transition metal oxalates under the same conditions for further comparison.

2.2 | Material Characterization

The pulverized samples were investigated by X-ray diffraction at room temperature on a Bruker D8-A25-Advance diffractometer in Bragg-Brentano θ-θ-geometry (goniometer radius 280 mm) with non-monochromatic Cu $K_{\alpha 1,2}$-radiation ($\lambda = 154.0596$ pm and 154.4425 pm). The powder was filled into the groove of a silicon zero-background sample holder, and the surface was flattened with a glass slide and flush with the edge of the sample holder for testing. Diffraction patterns were recorded between 7° and 120° 2θ with a step size of 0.013° and a total scan time of 2 h. A 12 μm Ni foil working as a K_β filter and a variable divergence slit were mounted at the primary beam side. On the secondary beam side, a LYNXEYE detector with 192 channels was used. The recorded data were evaluated using Bruker TOPAS 5.0 employing the fundamental parameter approach and the Rietveld method [28, 29].

The D8 Discover diffractometer (Bruker AXS) was employed to analyze the electrode before and after cycling. The copper X-ray source (Cu-K_α, $\lambda = 1.5406$ Å, 40 kV, 40 mA) was employed, coupled with a Göbel lens to achieve 1 mm spot focusing. Signal acquisition was performed using an EIGER2 two-dimensional detector, and data were collected over a 2θ range of 10°–80°. The measurements were carried out in continuous mode with an angular increment of 0.019° 2θ and a counting time of 1 s per step. Samples were placed on an optical glass sample holder with a depth of 0.5 mm for testing. All collected diffraction patterns underwent intensity normalization within the range 0–1.

Scanning electron microscopy (SEM) was performed using a ZEISS GEMINI 500 equipped with an EDS detector from Oxford Instruments. The samples were mounted on aluminum stubs using conductive carbon tape and sputter-coated with a thin platinum layer (~10 nm) to enhance conductivity and prevent charging during SEM observation. An accelerating voltage of 2 kV was employed for imaging and 10 kV for spectroscopy.

X-ray photoelectron spectroscopy (XPS) measurements were conducted using the K-Alpha XPS System from Thermo Scientific [30]. The photon source employed was a monochromatized Al K_α line with an energy of $h\nu = 1486.6$ eV. Spectra were captured using a spot size of 400 µm and a consistent pass energy. For charge neutralization, we utilized a combined low-energy electron/ion flood source. A dual monoatomic and gas cluster argon ion source is used for sample cleaning. The C 1 s peak was used for binding energy calibration and set to 284.8 eV for adventitious carbon.

Raman spectroscopy was performed using a Renishaw inVia Raman spectrometer [31]. The samples were pressed onto a glass slide for testing. The laser wavelength used was 532 nm, and the laser power at the sample's focal point was about 0.5 mW. For each measurement, an exposure time of 10 s was used, with 3 accumulations to improve the signal-to-noise ratio. Cosmic ray removal algorithms were applied during post-processing to eliminate spurious spikes from high-energy particle interference. To ensure the accuracy of the measurements, the system was calibrated using a silicon wafer before and after the measurements. The obtained data were normalized (0-1) to ensure consistency.

Thermogravimetric analysis (TGA) was performed using a Netzsch Libra TG 209 F1, with a heating rate of 10°C/min from 30°C to 600°C in argon.

Inductively coupled plasma-optical emission spectroscopy (ICP-OES) was performed on a Horiba Jobin Yvon Ultima2 instrument. For ICP-OES analysis, the samples were dissolved in hydrochloric acid and diluted with deionized water before measurement. The pressure of the nebulizer was 258 kPa, and the flow rate was set to 138 L/min.

2.3 | Electrode Preparation and Electrochemical Characterization

The TMOx-based electrodes consisted of active materials (70 mass%), acetylene black (AB, Thermo Scientific, 20 mass%), and a 3 mass% fraction of sodium carboxymethylcellulose solution in water as a binder (CMC 250 000, Sigma-Aldrich, 10 mass %). For slurry preparation, the active materials and AB were first mixed in a mortar, and then the CMC binder was added, and the mixture was milled using a FRITSCH PULVERISETTE 7 planetary micro mill at 500 rpm for 30 min. Then, the electrode slurry was cast onto copper foil (25 µm, MTI) using a laboratory doctor blade (150 µm wet film thickness). After drying in a vacuum at 80°C for 24 h, circular electrodes (12 mm in diameter) were punched out using a press-punch (EL-CELL). The active material loading ranged from 1.5 to 2.0 mg/cm^2.

The electrochemical performance was evaluated in CR2032 coin cells, using lithium metal as both the counter and reference electrodes. All cells were assembled in an argon-filled glovebox (MBraun LabMaster 130, [H_2O] and [O_2] < 0.1 ppm). The electrolyte consisted of a 1 M solution of $LiPF_6$ in ethylene carbonate/dimethyl carbonate (EC: DMC, 1:1 by volume; Sigma-Aldrich). For the cells, a glass fiber (GF/F, Whatman) separator was used. Galvanostatic cycling with potential limitation (GCPL), cyclic voltammetry (CV), and performance measurements were carried out using a VMP3 multi-channel potentiostat/galvanostat and a BCS-810 battery tester from Bio-Logic. Cyclic voltammetry was carried out in the voltage range of 0.01–3.0 V versus Li^+/Li with a scan rate of 0.1–2 mV/s. The galvanostatic charge/discharge cycling with potential limitation data was collected at voltages in the range of 0.01–3.0 V versus Li^+/Li. For all GCPLs in this work, a specific current of 100 mA/g was used unless stated otherwise. Electrochemical impedance spectroscopy (EIS) was measured at the formal potential in the frequency range of 100 kHz to 10 mHz with an amplitude of 5 mV. All electrochemical measurements were performed in climatic chambers with a set temperature of (25 ± 1)°C.

3 | Results and Discussion

3.1 | Material Characterization

Figure 1 shows the preparation process of multi-phase transition metal oxalates. When five transition metal chlorides are dissolved in water, hydrated transition metal ions $[M(H_2O)_6]^{2+}$ (M = Mn, Fe, Co, Ni, Cu) are formed, which usually present a regular six-coordinated octahedral structure [32, 33]. However, the Cu^{2+} ion will have a structural distortion due to the Jahn-Teller effect, showing a deformed octahedron with four water molecules in the plane having shorter distances and two water molecules in the axial direction having longer distances to the central atom [34, 35]. When oxalic acid is dissolved in water, it can dissociate forming $C_2O_4{}^{2-}$. As a strong chelating ligand, it can form a stable five-membered ring structure with transition metal ions through two oxygen atoms, gradually replacing the H_2O molecules in the hydrated transition metal ions [34], forming two similar structures, $MC_2O_4{\cdot}2H_2O$, with different elemental compositions. Cu^{2+} with a stronger affinity will precipitate in the form of water-free CuC_2O_4 after reaching its maximum substitution amount [36].

The phase composition and cell parameters of the samples were obtained from Rietveld analysis of the X-ray diffractograms (Figure 2A). The samples TMOx-0, TMOx-1, and TMOx-2 can all be described by the monoclinic structure of $Fe(C_2O_4){\cdot}2\,H_2O$, which adopts the space group $C2/c$ [37]. Rietveld fitting required the use of more than one phase. This is mainly due to a slight asymmetry in the line widths. This asymmetry becomes more pronounced at higher diffraction angles. Since a combination of different transition metals was used in the synthesis, it can be assumed that the phase separates into a variety of solid solutions. Therefore, two fractions with the same structural type were used to fit the data. Still, differences in lattice parameters were allowed to be refined (Figure 2A). Considering that the electron numbers of the used transition metal elements are very close to each other, it is not possible to distinguish them by XRD

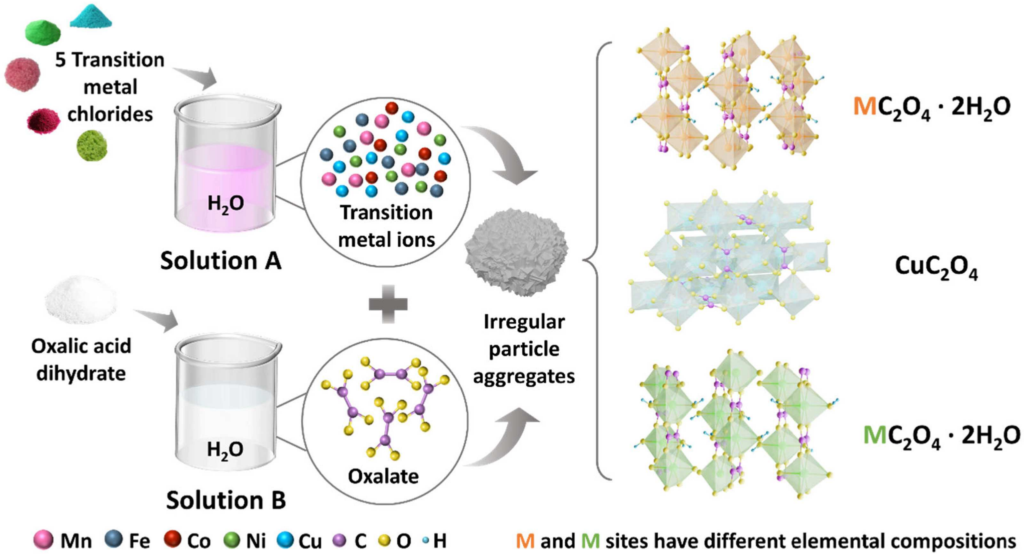

FIGURE 1 | Schematic illustration of the synthesis of multi-phase transition metal oxalates.

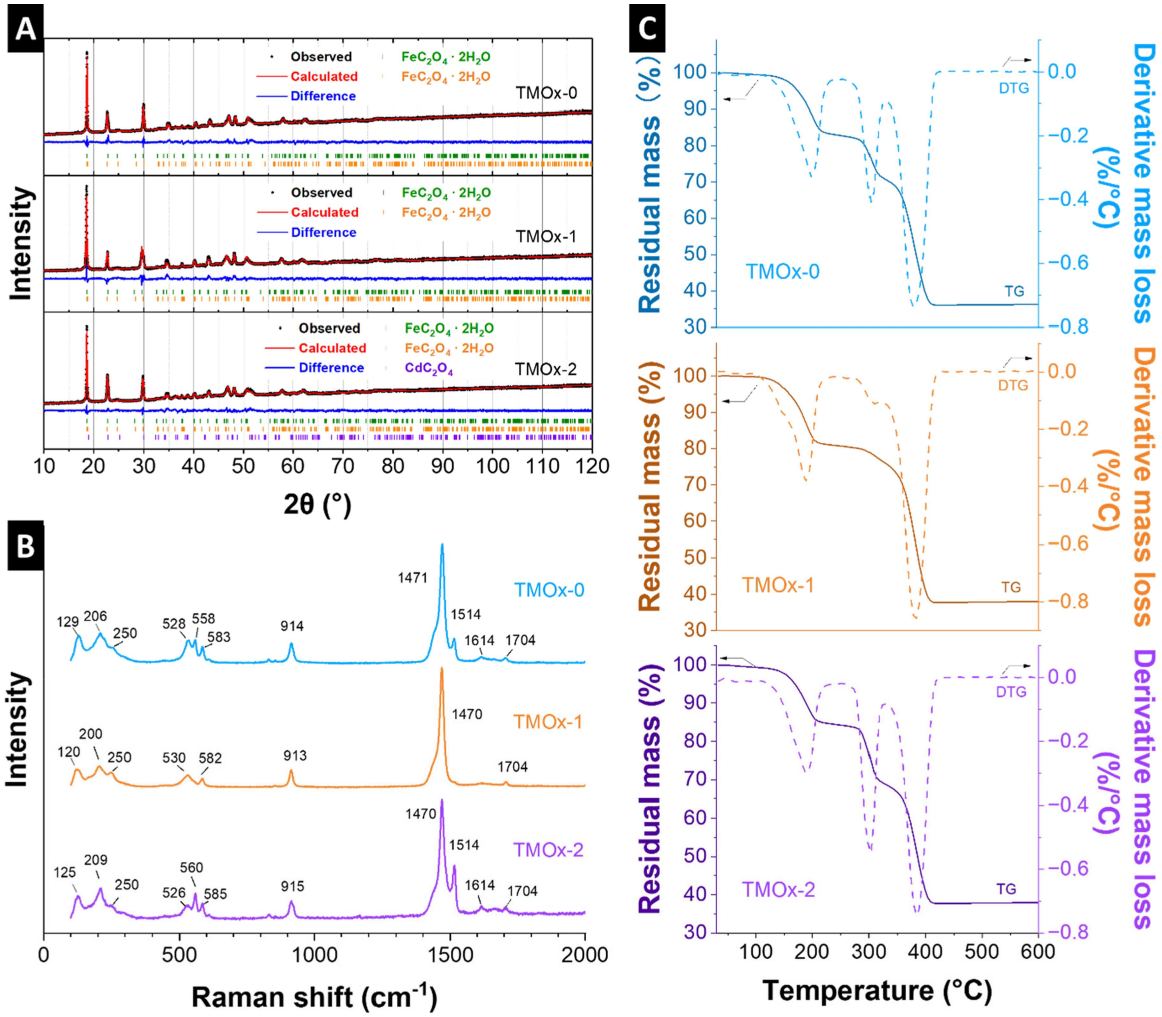

FIGURE 2 | Structure and thermal properties of the obtained multi-phase transition metal oxalates. (A) X-ray diffractograms, (B) Raman spectra, and (C) thermogravimetric and differential thermogravimetric data of TMOx-0, TMOx-1, and TMOx-2.

under these conditions [38]. Therefore, performing elemental analysis can only determine the overall composition of the sample; however, it cannot determine the composition of the individual phases in the two-phase region. The refined lattice parameters are presented in Supporting Information: Table S1, and differences in the cell parameters of the two phases, with a close percentage difference, can be observed in samples TMOx-0 and TMOx-1. This confirms our hypothesis that solid solutions with different elemental compositions are formed.

In addition, a third phase was found in the X-ray diffractogram of the TMOx-2 sample, which corresponds to the CdC_2O_4 type structure, again a monoclinic structure (space group $P2_1/c$) [39]. Ni and Cu have been reported to adopt this structure type [39, 40]. Combined with ICP-OES data, the content of each transition metal element in the sample was further analyzed. The results indicate that sample TMOx-2 contains an excess of copper compared to other samples (Supporting Information: Figure S2A). The existence of the third phase may be due to the maximum substitution of Cu being exceeded, which allows the remaining Cu atoms to precipitate as CuC_2O_4 (monoclinic $P2_1/c$ structure) [36]. TMOx-3 exhibits the monoclinic CdC_2O_4 type (space group $P2_1/c$; Supporting Information: Figure S1A) [39]. Although there is a small reflection at 74° 2θ that is not well fitted, it still provides useful insights into the formation of oxalate. When combined with EDS data, it contains only copper, confirming it as anhydrous copper oxalate (Supporting Information: Table S2). This is also evidenced by the significant color difference from other samples (Supporting Information: Figure S2B).

To further understand the structures of multi-phase transition metal oxalates, additional analysis was performed in conjunction with Raman spectroscopy. Figure 2B shows the Raman spectra of the samples TMOx-0, TMOx-1, and TMOx-2. The bands observed at 1470 and 1514 cm^{-1} are attributed to the C-O stretching mode [41], while the Raman peak at around 915 cm^{-1} is attributed to the C-C stretching vibration [42, 43]. The bands from 520 to 590 cm^{-1} correspond to the bending vibration of the δ ring, and the bands below 300 cm^{-1} mainly correspond to the vibration of the M-O bond [44]. These results are consistent with previously reported metal oxalates and confirm the formation of transition metal oxalates.

Figure 2C shows the thermal decomposition behavior of samples TMOx-0, TMOx-1, and TMOx-2 by TGA in the range of 30°C to 600°C. For all three samples, we see three consecutive mass loss ranges. The first decrease (below 250°C) corresponds mainly to the removal of the crystal water of the hydrated oxalate [45]. The second and third steps correspond to the decomposition of the oxalates (between about 250°C–450°C) [46]. In this multicomponent (Mn, Fe, Co, Ni, Cu) oxalate system, differences exist in the thermal stability and decomposition routes of oxalates from different transition metals. These differences in decomposition temperatures result in two distinct weight losses [13, 47]. The whole decomposition process can be categorized as dehydration and decarboxylation processes, and the reactions occurring are as follows:

$$MC_2O_4{\cdot}2H_2O \rightarrow MC_2O_4 + 2H_2O\ (M = \text{Mn, Fe, Co, Ni, Cu}) \tag{1}$$

$$MC_2O_4 \rightarrow MO + CO + CO_2\ (M = \text{Mn, Fe, Co, Ni, Cu}) \tag{2}$$

The morphology of the samples was analyzed by recording scanning electron micrographs (Figure 3A–F and Supporting Information: Figure S1D,E). TMOx-2 shows secondary particles in the range of 5–10 µm, which are generally believed to be formed by the aggregation of transition metal ions during the precipitation process (Figure 3C,F) [48]. Similarly, the morphology of TMOx-1 presents irregular aggregates around 5–10 µm (Figure 3B,E). In contrast to TMOx-1 and TMOx-2, TMOx-0 has a larger particle size, roughly 10–20 µm (Figure 3A,D). As for TMOx-3, due to the presence of only one single structure, it shows a special 2–5 µm flake-like morphology, which is also common for other copper oxalate particles (Supporting Information: Figure S1D,E) [49]. The elemental distribution of TMOx-0, TMOx-1, and TMOx-2 was evaluated by energy dispersive X-ray spectroscopy (EDS) elemental mapping. Figure 3G-L and Supporting Information: Figure S3 confirm that the five transition metal elements, Mn, Fe, Co, Ni, and Cu, are well distributed within the TMOx particles.

The presence of five transition metal elements on the sample surface was further investigated by high-resolution X-ray photoelectron spectroscopy (XPS; Figure 4 and Supporting Information: Figures S4–S6). Figure 4 depicts the deconvoluted X-ray photoelectron spectra of Mn 2p, Fe 2p, Co 2p, Ni 2p, Cu 2p, and O 1 s in their respective energy regions observed for the TMOx-2 sample. As shown in Figure 4B, the peaks at 642.9 and 654.1 eV in the Mn 2p spectrum can be attributed to Mn $2p_{3/2}$ and Mn $2p_{1/2}$ in the divalent state [50, 51]. The characteristic Fe 2p peaks appeared at 710.8 eV (Fe $2p_{3/2}$) and 723.9 eV (Fe $2p_{1/2}$) in Figure 4C, with a spin energy separation of 13.1 eV, indicating the divalent oxidation state [52]. The spectrum of Fe $2p_{3/2}$ for the TMOx-0 sample (Supporting Information: Figure S4C) consists of Fe^{3+} (714.6 eV) and Fe^{2+} (710.7 eV), and the spectrum of Fe $2p_{1/2}$ also consists of Fe^{3+} (727.7 eV) and Fe^{2+} (723.8 eV), suggesting the coexistence of Fe^{3+} and Fe^{2+} [53]. In Figure 4E, the Ni 2p spectra show main peaks at 856.6 eV (Ni $2p_{3/2}$) and 874.5 eV (Ni $2p_{1/2}$) and satellite peaks at higher binding energies, which are typical of Ni^{2+} [54, 55]. For TMOx-0, the Ni 2p spectra (Supporting Information: Figure S4E), in addition to the main peaks at 856.7 eV (Ni $2p_{3/2}$) and 874.4 eV (Ni $2p_{1/2}$), show a pair of weak peaks at 853.5 eV (Ni $2p_{3/2}$) and 870.8 eV (Ni $2p_{1/2}$), indicating the presence of a small amount of Ni^0, which could have been produced by X-ray irradiation during XPS [51]. Similarly, the Co 2p peaks at 782.3 and 798.1 eV relate to Co $2p_{3/2}$ and Co $2p_{1/2}$, and the satellite peaks were also detected at 787.1 and 803.1 eV (Figure 4D), indicating the presence of Co^{2+} [55, 56]. For Cu 2p in Figure 4F, peaks at 933.2 and 952.9 eV were attributed to Cu $2p_{3/2}$ and Cu $2p_{1/2}$, indicating the presence of Cu^{2+} [51, 56]. In addition, two other peaks at 933.0 and 952.9 eV appear in the Cu 2p spectrum of TMOx-3 (Supporting Information: Figure S6C), corresponding to Cu^{1+} $2p_{3/2}$ and Cu^{1+} $2p_{1/2}$, respectively, which are Cu^{1+} chemical states due to the apparent degradation of copper oxalate by X-rays [55].

3.2 | Electrochemistry

To further explore the electrochemical performance, cyclic voltammetry measurements were performed on the oxalate-based

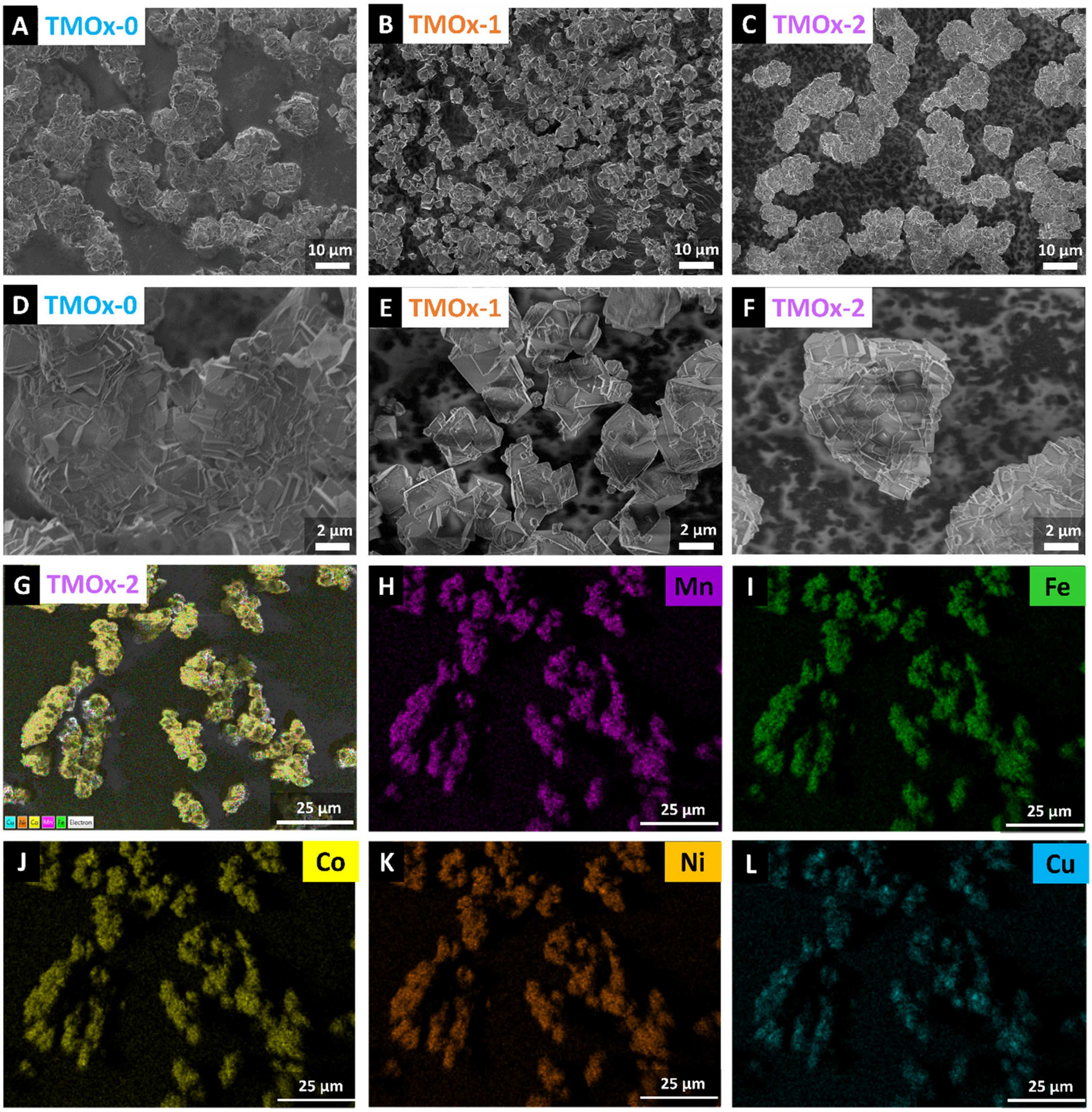

FIGURE 3 | Morphology of the obtained multi-phase transition metal oxalates. (A, D) Scanning electron micrographs of TMOx-0, (B, E) Scanning electron micrographs of TMOx-1, (C, F) Scanning electron micrographs of TMOx-2, and (G-L) Elemental EDS mapping of TMOx-2.

electrodes. Figure 5A–D shows the cyclic voltammograms for the first five cycles obtained at a scan rate of 0.1 mV/s in the 0.01-3.00 V versus Li^+/Li. For the TMOx-0, TMOx-1, and TMOx-2 electrodes (Figure 5A–C), two reduction peaks (R1 and R2) are observed in the first cycle, located at approximately 0.90 V versus Li^+/Li and 0.45 V versus Li^+/Li. The R2 peak at about 0.90 V versus Li^+/Li can be attributed to electrolyte reductive decomposition and polymeric solid electrolyte interphase (SEI) formation [57]. The R1 peak at about 0.45 V versus Li^+/Li can be attributed to the conversion of M^{2+} to M^0 and $\text{Li}_2\text{C}_2\text{O}_4$ [15], which is also commonly found in other single-phase transition metal oxalates, as shown in Equation (3) [11, 52, 58]:

$$MC_2O_4 + 2\text{Li}^+ + 2e^- \leftrightarrow M + \text{Li}_2C_2O_4 \tag{3}$$

$$(M = \text{Mn, Fe, Co, Ni, Cu})$$

In the subsequent anodic scan, an oxidation peak (O1) appears at 1.0 V versus Li^+/Li, possibly corresponding to the partial SEI delithiation. In comparison, the subsequent broad oxidation peak (O2 and O3) at 1.3–1.7 V versus Li^+/Li corresponds to the redox reaction of multiple electrode pairs (M^0 is oxidized to M^{2+}). After the initial scanning process, the R2 peak at 0.9 V versus Li^+/Li disappears completely, indicating that the SEI gradually forms mainly in the first cycle. A new reduction peak appears between 1.0 V versus Li^+/Li and 1.5 V versus Li^+/Li, moving to lower voltages with increasing cycling number. This may be attributed to the activation and polarization of the electrode with repeated cycles [59]. The O1 peak at 1.0 V versus Li^+/Li is gradually getting weaker, while the subsequent broad oxidation peak position remains unchanged. These results indicate that the electrochemical lithium storage of $MC_2\text{O}_4$ electrodes involves multi-step lithium reactions.

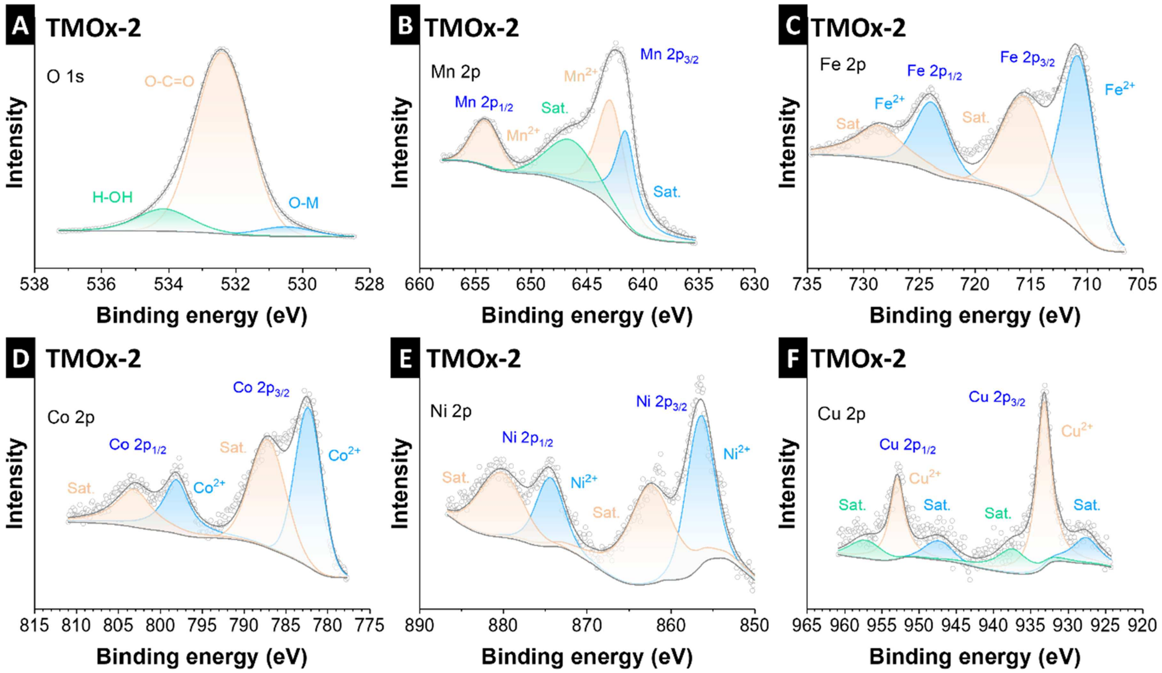

FIGURE 4 | High-resolution X-ray photoelectron spectra of TMOx-2. (A) O 1s, (B) Mn 2p, (C) Fe 2p, (D) Co 2p, (E) Ni 2p, and (F) Cu 2p.

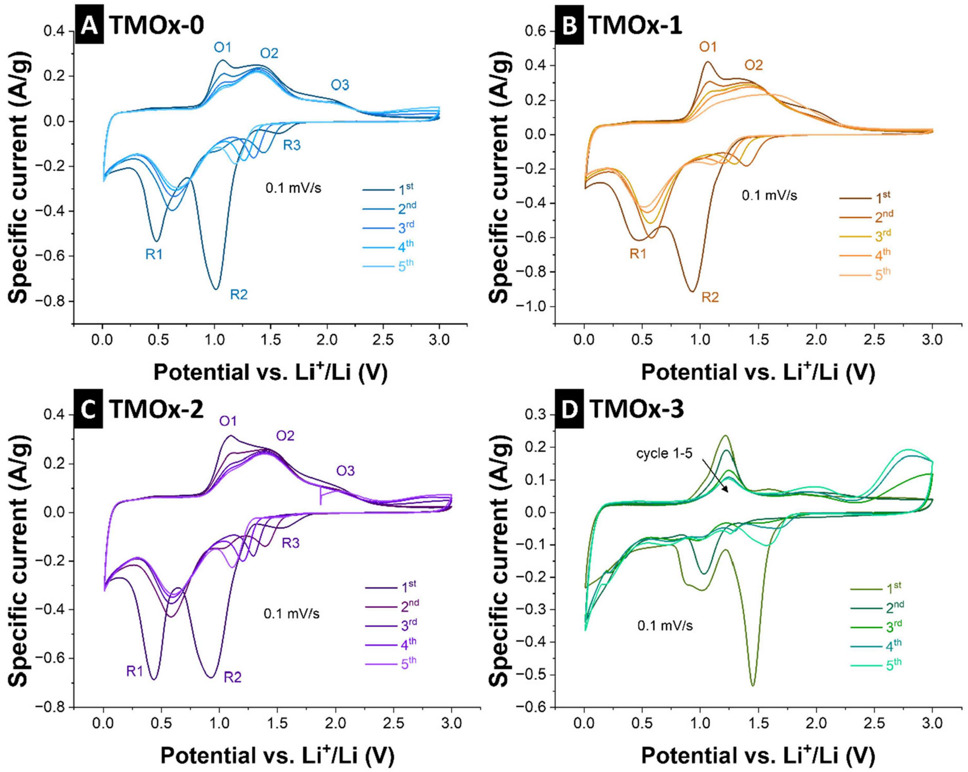

FIGURE 5 | Cyclic voltammograms of the prepared transition metal oxalates at a scan rate of 0.1 mV/s. (A) TMOx-0, (B) TMOx-1, (C) TMOx-2, and (D) TMOx-3.

As for the TMOx-0 and TMOx-2 electrodes (Figure 5A,C), a weaker reduction peak (R3) at about 1.54 V versus Li^+/Li was observed, which may be related to the presence of a large amount of copper ions. By comparing with the single-phase copper oxalate electrode in Figure 5D, which also shows a reduction peak at the same potential, the typical conversion reaction is illustrated in Equations (4–5). Additionally, a distinct oxidation peak appeared at 2.65 V versus Li^+/Li in the 3rd cycle. Its intensity gradually increased with further cycling, and its redox reaction could be attributed to the reversible reaction of

Cu_2O and Li_2CuO_2 according to the principle of electrode potential [52, 60], as shown in Equation (6):

$$CuC_2O_4{\cdot}xH_2O + Li^+ + e^- \rightarrow Cu_2O + Cu + Li_2CO_3 + Li_2O + LiOH \tag{4}$$

$$2Cu + Li_2O \leftrightarrow Cu_2O + 2Li^+ + 2e^- \tag{5}$$

$$Cu_2O + 3Li_2O \leftrightarrow 2Li_2CuO_2 + 2Li^+ + 2e^- \tag{6}$$

For multi-phase transition metal oxalates, we observed significant changes in peak potentials relative to single-phase transition metal oxalates. After several cycles, the peak potentials of the redox pairs of different transition metal elements shifted significantly to closer intermediate potential values, thus producing a more continuous and smoother response than each redox pair alone. These changes may be caused by the interaction of the nanocomposites formed during the first few cycles, resulting in a beneficial synergistic effect on the properties of these materials [61].

The electrochemical reaction mechanism was further studied by analyzing galvanostatic charge/discharge curves with potential limitation. Figure 6 shows the discharge-charge curves of TMOx-0, TMOx-1, TMOx-2, and TMOx-3 at a specific current of 100 mA/g for different cycles in the potential range of 0.01–3 V versus Li^+/Li. Among them, TMOx-0, TMOx-1, and TMOx-2 electrodes exhibit similar Li^+ insertion/extraction trends. The first lithiation curves of all three samples feature mainly three pronounced plateaus at around 1.3 V versus Li^+/Li, 0.9 V versus Li^+/Li, and 0.6 V versus Li^+/Li, characterizing the conversion reaction but also the irreversible contribution to the SEI formation. Compared to the TMOx-3 electrode, which has a long plateau between 1.7 V versus Li^+/Li and 1.3 V versus Li^+/Li, the TMOx-0 and TMOx-2 electrodes in the same potential show much shorter plateaus, which can be related to the presence of a large amount of Cu^{2+} in the samples and therefore extended species to be reduced. The sharp drop in its electrode potential belongs to the electrochemical reaction of MC_2O_4 and lithium to form $Li_xMC_2O_4$ [62]. The flat plateau from 1.3 V versus Li^+/Li to 0.5 V versus Li^+/Li can be attributed to the conversion reaction of multiple transition metal elements (from M^{2+} reduction to M^0). In the following cycles, the material shows a slope instead of a plateau during lithiation, which is attributed to the varying charge/discharge potentials of different transition metals and the structural rearrangements that occur during the cycle [63]. The slope below 0.5 V versus Li^+/Li corresponds to the pseudocapacitive behavior of the polymer surface gel layer and the interfacial lithium storage behavior [13]. The de-lithiation curves of the electrode show plateaus around 0.9 V versus Li^+/Li and 2.4 V versus Li^+/Li connected with a slope, characterizing the overlapping of redox features of different transition metals at specific potentials. During the first de-lithiation, the potential of all samples rose rapidly to about 1 V versus Li^+/Li. Subsequently, a narrow plateau period occurs with capacities up to 900 mAh/g. Eventually, it rises rapidly to 3 V versus Li^+/Li, suggesting a large irreversible loss of capacity during the first cycle, characterizing the process of SEI formation [11].

To systematically clarify the charge storage kinetics of oxalate electrode materials, quantitative analysis of current responses was conducted based on cyclic voltammetry at different scan rates (Figure S7). The peak current i exhibits the following relationship with scan rate ν, as below Equation 7 [64]:

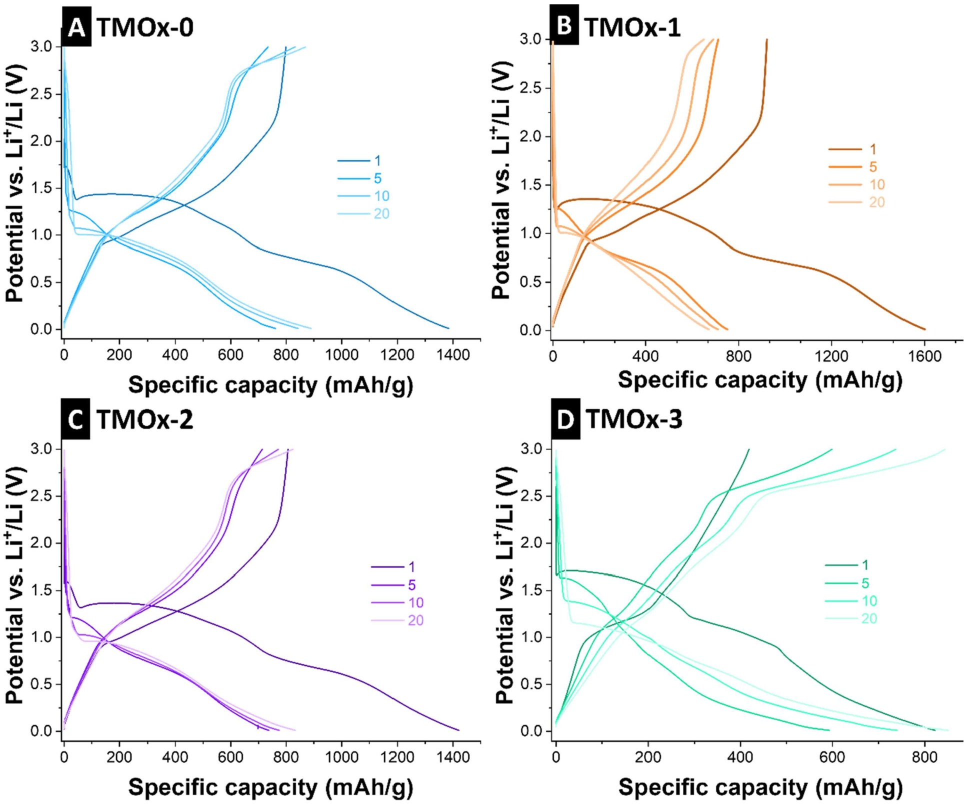

FIGURE 6 | Galvanostatic charge and discharge profiles at 100 mA/g for (A) TMOx-0, (B) TMOx-1, (C) TMOx-2, and (D) TMOx-3.

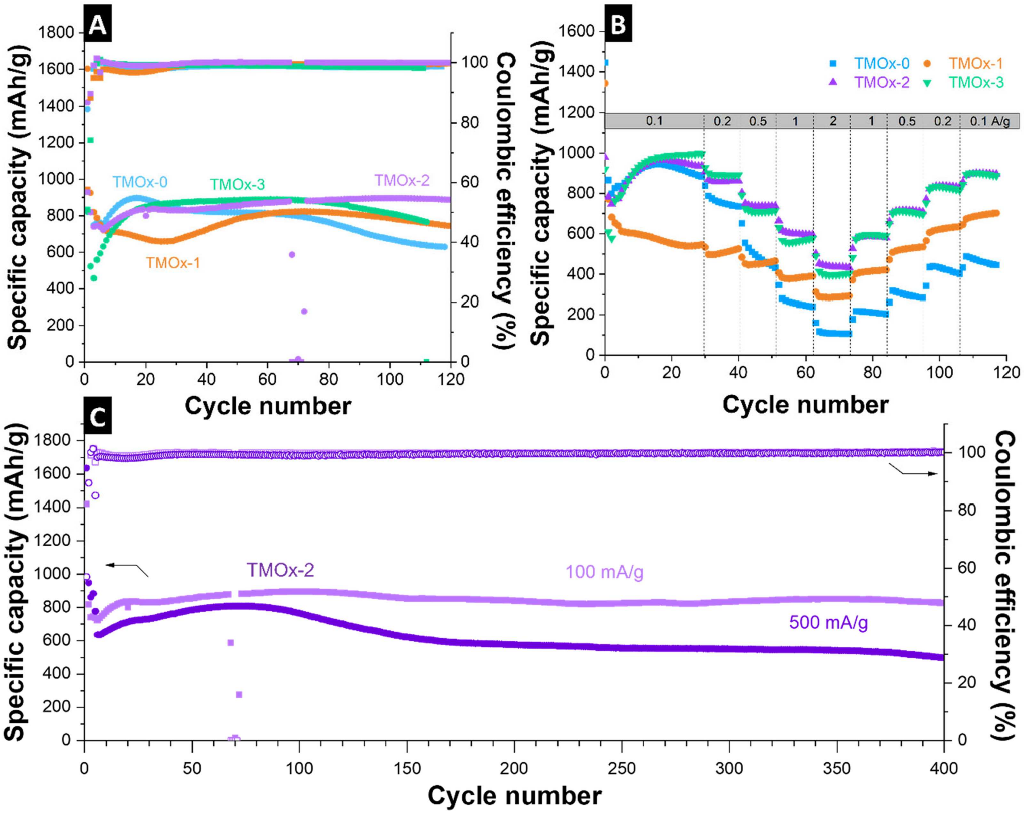

FIGURE 7 | (A) Galvanostatic charge/discharge cycling stability at 100 mA/g with corresponding Coulombic efficiency. (B) Rate handling ability during galvanostatic charge/discharge cycling at different rates. (C) Long-term cycling performance of TMOx-2 electrodes at rates of 100 mA/g and 500 mA/g.

$$i = a\nu^{b} \tag{7}$$

where the b value reflects the dominant charge storage mechanism. When b approaches 0.5, it indicates diffusion-controlled electrochemical reactions, as common for battery-like ion intercalation or conversion reactions. In contrast, a non-diffusion-limited charge transfer process would correspond with a b-value close or equal to 1.0; such values are typical for capacitive energy storage dominated by surface limitations [57]. A series of b values were obtained by fitting the cyclic voltammograms of the oxalate electrode in the scan rate range of 0.2–2 mV/s. For the oxidation process, the b values obtained for the three multiphase transition metal oxalate electrodes TMOx-0, TMOx-1, and TMOx-2 were 0.63, 0.5, and 0.58, respectively. This value indicates that although ion extraction is primarily limited by diffusion within the oxalate framework, surface redox sites also contribute. Due to the broad cathodic response at high scan rates, reduction kinetic analysis was conducted at a fixed potential of 0.4 V, where the b values obtained were 0.78, 0.56, and 0.73. At this potential, the contribution from surface-induced storage becomes more significant. The obtained b-value range ($0.5 < b < 1.0$) confirms that the oxalate electrode operates via a mixed charge storage mechanism.

Based on these results, the current response was further quantitatively separated into capacitive and diffusion contributions. The total current can be expressed as the combination of surface capacitive behavior and diffusion-controlled ion intercalation, described by the following Equations 8 and 9 [65]:

$$i(V) = k_1\nu + k_2\nu^{1/2} \tag{8}$$

$$i(V)/\nu^{1/2} = k_1\nu^{1/2} + k_2 \tag{9}$$

where k_1 and k_2 represent the surface non-diffusion-limited contribution and diffusion-controlled contribution constants at a fixed potential V, respectively. By performing a linear fit of $i(V)/\nu^{1/2}$ versus $\nu^{1/2}$, the proportion of non-diffusion-limited contribution at different scan rates can be quantified. Our data show that the non-diffusion-limited contribution to the total capacity continuously increases with rising scan rates, for TMOx-2 electrode, reaching approximately 83% at 2 mV/s.

The cycling stability and rate performance of several transition metal oxalate electrodes are shown in Figure 7A–C. Figure 7A displays the cycling performance of the TMOx-0, TMOx-1, TMOx-2, and TMOx-3 anodes at 100 mA/g. The initial Coulombic efficiencies of the TMOx-0, TMOx-1, TMOx-2, and TMOx-3 samples are 58%, 58%, 57%, and 51%, respectively. The lower initial Coulombic efficiencies can be attributed to the electrolyte reduction/SEI formation [16, 66], formation and partial decomposition of $Li_2C_2O_4$, trapped Li-ions in interphases/defects sites, and parasitic reactions with crystal water [67, 68]. During the following cycles, it reaches almost 100%, which is mainly due to the progressive wetting, increased electronic percolation via in-situ generated metallic phases (e.g., Cu^0), and growth/stabilization of a conductive polymeric/gel interphase [13]. At the same time, the presence of a small amount of crystal water and the inevitable volume expansion may also promote the structural instability during the Li^+ insertion/extraction process [16]. With the progression of the initial activation cycles, an increasing fraction of electrochemically addressable species, especially M^0 nanometals, is gradually activated. As a result, more electrons participate in the conversion reaction, giving rise to a progressive increase in capacity that stabilizes after around 20 cycles [57].

For the TMOx-0 anode, the capacity has decayed after nearly 20 cycles. This also happens in the TMOx-1 sample, where the initial capacity is lower compared to the others. This can be explained by the different compositions of the samples with TMOx-1 sample containing more iron, which compared with the presence of large amounts of copper in other samples, often delivers lower initial capacity [11, 60]. The capacity decay of the two samples in the following cycles is mainly due to the instability of the composite of two monoclinic oxalate structures, which causes rupture, particle pulverization, or morphology collapse during Li^+ insertion/extraction, further weakening the conductive path and active interface, thereby reducing the capacity retention ability [43, 69]. TMOx-3 exhibited good cycling stability after achieving the highest capacity of 870 mAh/g after 25 cycles, but significant capacity decay was observed after reaching 90 cycles. TMOx-2 exhibits good cycling stability, maintaining a high discharge capacity of 887 mAh/g after 120 cycles. These results clearly indicate that the synergistic effect of the three structures plays an important role in determining the electrochemical performance of transition metal oxalates [70].

Figure 7B shows the rate performance of TMOx-0, TMOx-1, TMOx-2, and TMOx-3 electrodes at different rates between 0.01 V versus Li^+/Li and 3 V versus Li^+/Li. Considering the growth and stabilization of a conductive polymeric/gel interphase, the battery was first cycled at 100 mA/g for 30 cycles, then cycled at 200 mA/g, 500 mA/g, 1 A/g, and 2 A/g, and finally gradually recovered to 100 mA/g. The discharge specific capacity of the TMOx-0 electrode decreased significantly with specific current, reaching only about 105 mAh/g at 2 A/g, while being unstable at the same rate. After high-rate cycling, the specific capacity decreased significantly when the rate was restored to 100 mA/g, which may be due to SEI thickening under high overpotential, loss of electronic percolation (pulverization), and Li-ion trapping [71, 72].

The discharge capacity of the TMOx-1 electrode also decreases with the increase in the rate. Although there is no capacity decay after returning to a low current, its discharge capacity is always low. TMOx-2 exhibits high discharge capacity at different rates, with discharge capacities of 860 mAh/g, 736 mAh/g, 600 mAh/g, and 438 mAh/g at 200 mA/g, 500 mA/g, 1 A/g, and 2 A/g, respectively. After the rate handling test, when the rate returned to 100 mA/g, the capacity also recovered to 900 mAh/g, and there was no decay in the following 10 cycles. This phenomenon reflects the beneficial structural flexibility and stability of the TMOx-2 electrode. Compared with the TMOx-2 electrode, the TMOx-3 electrode showed very similar behavior but a slight capacity decay, which was primarily attributed to the instability of its single monoclinic structure. The improvement of the rate performance of the TMOx-2 electrode was mainly attributed to the synergistic effect of the $MC_2O_4{\cdot}2H_2O$-CuC_2O_4-$MC_2O_4{\cdot}2H_2O$ multiphase structure, which provides a relatively stable framework, thereby effectively improved the transport of electrons and ions in the electrode [72].

In addition, the effect of multi-phase synergy on structural stability and ion transport in the TMOx-2 sample was further confirmed by the long-term cycling performance of 400 cycles at 100 and 500 mA/g, respectively (Figure 7C). At a low specific current of 100 mA/g, the TMOx-2 electrode has good cycling performance and still achieves a high capacity of 827 mAh/g after 400 cycles. The lower current reduces polarization and allows diffusion to keep pace, enabling deeper, more complete conversion with less stress. Meanwhile, the smoothness of the path is the main factor determining electrochemical performance at high currents [12]. At a higher specific current of 500 mA/g, the capacity of TMOx-2 exhibits a slow decline after approximately 80 cycles, which may be attributed to irreversible defects in the crystal structure resulting from rapid Li^+ transport [12]. After 400 cycles, the discharge capacity remains at about 500 mA/g. This good rate capability and long-term cycling performance can be attributed to the synergistic effect between the two $MC_2O_4{\cdot}2H_2O$ and CuC_2O_4 components. Specifically, the presence of Cu enhances electronic conductivity, while the multiphase structure composed of different transition metal oxalates provides a stable framework for the transport of electrons and ions. Within this framework, Cu is embedded as a conductivity enhancer into a stable multiphase matrix, and the synergistic effect of the two results in good cycling stability during long-term cycling.

Compared with other transition metal oxalate materials exhibiting high lithium storage performance, the TMOx-2 electrodes deliver moderate reversible capacity and capacity retention (Table 1). Unlike strategies that rely on introducing highly conductive additives (such as reduced graphene oxide), this work demonstrates a simple and effective way to improve the electrochemical lithium storage performance of transition metal oxalates by constructing multiphase structures.

EIS was used to analyze the charge transfer kinetics of the TMOx-0, TMOx-1, TMOx-2, and TMOx-3 electrodes. For comparison, EIS measurements were performed on the fresh cell at open-circuit potential and on the cycled cell after 100 cycles at the discharged state. Figure 8A,B shows the corresponding Nyquist plots for all electrodes in the frequency range of 100 kHz to 0.01 Hz, respectively. In the high-frequency region, the real axis intercept of the Nyquist plot represents the equivalent series resistance (R_{ESR}) of the cell, representing the electrolyte ionic resistance, the substrate intrinsic resistance, and the contact resistance at the active material/current collector interface [47]. The high-frequency region of the semicircle reflects the resistance to charge transfer at the electrode–electrolyte interface, commonly described as the surface film resistance (R_{SEI}). The mid-frequency region corresponds to the charge transfer resistance (R_{ct}) [59], while the low-frequency linear response is attributed to the solid-state diffusion of Li^+ within the active material, here we use the modified diffusion element M_α to explain the anomalous behavior.

For comparison, these Nyquist plots were fitted according to the equivalent circuit shown in the insets of Figure 8A,B, and all relevant parameters R_{ESR}, R_{SEI}, Q_{SEI}, R_{ct}, Q_{ct}, M_α, and Q were annotated [59].

Based on the quantitative impedance parameters obtained from EIS fitting (Supporting Information: Table S3), the reasons for

TABLE 1 | A comparison of electrochemical performance data for transition metal oxalates materials.

Material	Electrode composition	Capacity (mAh/g)	Cycle number	Specific current (mA/g)	Ref.
FeC_2O_4	AM: Super P: PVDF, 60: 30: 10	1326	100	373†	[73]
FeC_2O_4@Ge	AM: Super P: PVDF, 60: 30: 10	1090	200	1000	[74]
$Ni_{0.5}Co_{0.5}C_2O_4{\cdot}2H_2O$/rGO	AM: carbon black: PVDF, 80: 10: 10	1180	300	500	[75]
$FeCuC_2O_4{\cdot}2H_2O$@ $CuC_2O_4{\cdot}xH_2O$	AM: Super P: PVDF, 60: 30: 10	550 520	20 200	100 500	[52]
$FeC_2O_4{\cdot}2H_2O$	AM: Super P: PVDF, 60: 30: 10	450	500	500	[16]
$CuC_2O_4{\cdot}xH_2O$	AM: acetylene black: sodium alginate, 70: 20: 10	970 810	100	200 500	[60]
$CoC_2O_4{\cdot}2H_2O$/rGO	AM: carbon black: PVDF, 80: 10: 10	1012	200	200	[46]
$MC_2O_4{\cdot}2H_2O$ - CuC_2O_4 - $MC_2O_4{\cdot}2H_2O$	AM: acetylene black: CMC, 70: 20: 10	827 498	400	100 500	This work

†= recalculated from a value of 1 C, based on the theoretical specific capacity of FeC_2O_4, see Ref [76]. for the methodology.

the good electrochemical performance of the TMOx-2 electrode are revealed from a kinetic perspective. The initial R_{ct} of TMOx-2 is only 30.3 Ω, significantly lower than that of the single-metal reference sample TMOx-3 (395.7 Ω), indicating that it has good interfacial charge transfer kinetics. This significantly reduced R_{ct} may be due to the synergistic effect of the multi-metal cations in TMOx-2, which lowers the activation energy of electronic transitions between metal sites, thereby accelerating the interfacial reaction rate [77]. Although the R_{ESR} of all samples are at a low level (1.34–3.53 Ω), the higher initial R_{SEI} of TMOx-1 (253.8 Ω) indicates that it formed a relatively thicker or denser passivation film in the initial cycling stage.

Further comparison of the impedance evolution after 100 cycles reveals significant differences in interface stability and structural integrity among the different electrodes. For TMOx-2, its R_{SEI} remained almost unchanged, only from 103.5 Ω to 106.6 Ω, indicating that this electrode formed a stable SEI film during repeated lithium insertion/extraction. In contrast, TMOx-0 exhibited significant interfacial impedance accumulation after cycling, with its R_{SEI} increasing from 57.76 Ω to 135.6 Ω, while R_{ct} sharply rose from 140.2 Ω to 464.9 Ω. This reflects continuous thickening of the SEI film and severe suppression of charge transfer dynamics [14]. Furthermore, the R_{ESR} values of TMOx-1 and TMOx-3 increased significantly after cycling (reaching 16.85 Ω and 17.01 Ω, respectively), further suggesting that their overall electrode structure degraded. Due to its ability to simultaneously maintain low R_{ct} and stable R_{SEI} during long-term cycling, TMOx-2 achieves conversion reactions with low polarization, enabling higher reaction reversibility and faster kinetic response [78]. These results demonstrate that the multiphase structure design of TMOx-2 significantly enhances the electronic transport capability of the material, enabling it to maintain good interface dynamics during long-term cycling, thus exhibiting good cycling stability and rate performance.

To further explore the intrinsic relationship between the electrochemical performance and the structural and phase composition of the electrode material, we performed X-ray diffraction and SEM on the electrode material before and after cycling (Supporting Information: Figures S8 and S9).

As shown in Supporting Information Figure S8A,B, X-ray diffractogram of the mixed transition metal oxalate anode material before cycling revealed distinct diffraction peaks corresponding to the $Fe_2C_2O_4 \cdot 2H_2O$ crystal structure, indicating a well-defined crystalline structure in the initial material. Scanning electron micrographs further demonstrated regular geometric morphology (Supporting Information: Figure S9A, C, E, and G). X-ray diffractogram after cycling (including 3 cycles and 100 cycles) is shown in Supporting Information: Figure S8C–F. We observed the vanishing of the original oxalate diffraction peaks, with the predominant appearance of characteristic diffraction peaks from Li_2CO_3 and metallic diffraction peaks from the copper current collector. Although the theoretical products should include metallic elements and lithium oxalate, under the complex electrolyte interface environment, nanoscale metal particles exhibit strong catalytic properties, inducing the products to evolve into the more stable Li_2CO_3 [79]. The metal nanoparticles generated by the conversion reaction are highly dispersed in the amorphous matrix as extremely small clusters. Such minute grains cause the reflections to broaden to the background level [61]. This explains why the detected product

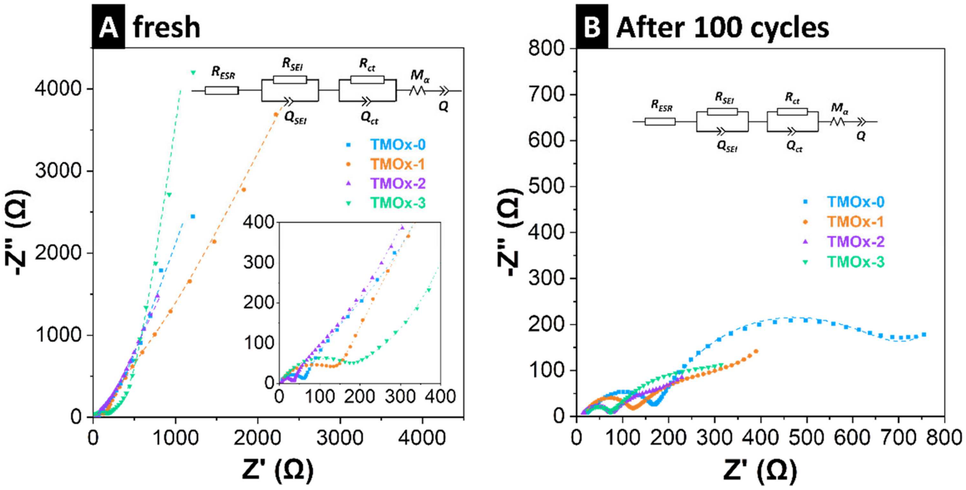

FIGURE 8 | Nyquist plots of (A) fresh cell, and (B) after 100 cycles at 100 mA/g. The inset shows the equivalent circuit used for the fit.

only showed Li_2CO_3. Furthermore, the appearance of Li_2CO_3 diffraction features can also be attributed to the formation of the solid electrolyte interface (SEI) during the initial cycling phase [80]. Meanwhile, scanning electron micrographs of the cycled electrode revealed its surface was uniformly coated with a thin film, (Supporting Information: Figure S9B, D, F, and H), which also confirms the formation of the SEI film after cycling.

Additionally, to further demonstrate the advantages of multi-phase transition metal oxalates, we also used the same preparation method to synthesize several single transition metal oxalates under the same conditions for comparison and tested their electrochemical performance. Supporting Information: Figure S10 shows the galvanostatic charge and discharge profiles and cycling performance of several single transition metal oxalates and the multi-phase transition metal oxalate electrodes prepared in this work at a rate of 100 mA/g. As can be seen in Supporting Information: Figure S10D, all transition metal oxalates exhibit good cycling stability. For the $MnC_2O_4 \cdot 2H_2O$ and $FeC_2O_4 \cdot 2H_2O$ electrodes, their initial capacities are only approximately 200 and 500 mAh/g, respectively. Although these capacities increase with cycling, they are still only around 300 mAh/g and 600 mAh/g after 100 cycles. As for $CoC_2O_4{\cdot}2H_2O$, it has high specific capacity and high cycle stability, maintaining a discharge specific capacity of 994 mAh/g after 100 cycles. However, due to the uneven distribution of cobalt reserves and its scarcity, cobalt prices have remained high and volatile, increasing battery costs and supply chain risks [81]. For our TMOx-2 electrode, the amount of cobalt was reduced by 90% during the synthesis process, and it still achieved a specific capacity of 895 mAh/g after 100 cycles, with good cycle stability, while effectively reducing the cost of the synthesis process.

Our work investigates transition metal oxalates with multiphase structures, maintaining high specific capacity and good cycling stability while reducing costs. However, structural optimization alone cannot completely solve the inherent problem of irreversible capacity loss in the first cycle of transition metal oxalate materials, and therefore requires further attention. In this context, complementary strategies such as pre-lithiation and surface modification can effectively compensate for irreversible lithium consumption and suppress parasitic interfacial reactions, thereby further improving initial coulombic efficiency [82, 83]. In conclusion, combining advanced structural design with pre-lithiation or surface engineering is a promising direction for reducing first-cycle capacity loss and accelerating the practical application of TMOx electrode materials in future LIBs.

4 | Conclusions

In summary, this study successfully synthesized a multi-phase transition metal oxalate material for lithium-ion battery anodes using a simple co-precipitation method. By adjusting the ratios of five transition metal elements, composite systems with different structural compositions were obtained. The results indicate that the multi-phase structure ($MC_2O_4{\cdot}2H_2O\text{-}CuC_2O_4\text{-}MC_2O_4{\cdot}2H_2O$) endows the material with a more stable framework, effectively alleviating structural collapse during cycling. Additionally, this framework facilitates the formation of continuous ionic channels, significantly enhancing ionic transport capability. In electrochemical testing, the prepared material exhibited high-rate performance and cycling stability, with remaining capacities of 827 mAh/g and 498 mAh/g after 400 cycles at rates of 100 mA/g and 500 mA/g, respectively. The performance improvement stems from the synergistic effect between the improved conductivity caused by Cu derived from CuC_2O_4 and the stable framework from the multiphase structure, as well as the collective promotion of electron transport and rapid charge compensation processes by multiple electrochemically active metals.

This study provides insights into the application of multi-phase metal oxalates in high-performance energy storage materials. Future research will further explore their comprehensive performance and mechanisms within full battery systems.

Author Contributions

Liying Xue: investigation, material synthesis, electrochemical testing and analysis, data curation, visualization, writing – original draft, writing – review and editing. **Stefanie Arnold:** validation, writing – review and editing. **Jean Gustavo de Andrade Ruthes:** electrochemical impedance spectroscopy analysis, writing – review and editing. **Oliver Janka:** X-ray diffractograms testing and analysis, data curation, visualization, writing – review and editing. **Chaochao Dun:** X-ray photoelectron spectra testing, data curation, writing – review and editing. **Volker Presser:** conceptualization, supervision, validation, resources, visualization, writing – original draft, writing – review and editing, project administration, funding acquisition.

Acknowledgments

L.X. acknowledges funding from the China Scholarship Council (CSC) via award number 202206660002. Instrumentation and technical assistance for this work were provided by the Service Center X-ray Diffraction, with financial support from Saarland University and German Research Foundation (project number INST 256/349-1). Work at the Molecular Foundry was supported by the Office of Science, Office of Basic Energy Sciences, of the U.S. Department of Energy under Contract No. DE-AC02-05CH11231. V.P. and S.A. acknowledge the support of the state government of Saarland within the framework of the En-FoSaar project, funded by the Saarland Transformation Program for Research and Knowledge Transfer (Transformationsprogramm Forschung und Wissenstransfer Saar). We thank the INM Service Group Chemical Analytics for the chemical analysis. Open Access funding enabled and organized by Projekt DEAL.

Conflicts of Interest

The authors declare no conflicts of interest.

Data Availability Statement

Data for this article are available at zenodo via https://doi.org/10.5281/zenodo.18494126.

References

1. M. Wakihara, “Recent Developments in Lithium Ion Batteries,” *Materials Science and Engineering: R: Reports* 33, no. 4 (2001): 109–134.

2. P. G. Bruce, B. Scrosati, and J. M. Tarascon, “Nanomaterials for Rechargeable Lithium Batteries,” *Angewandte Chemie International Edition* 47, no. 16 (2008): 2930–2946.

3. P. Roy and S. K. Srivastava, “Nanostructured Anode Materials for Lithium Ion Batteries,” *Journal of Materials Chemistry A* 3, no. 6 (2015): 2454–2484.

4. K. Yuan, Y. Lin, X. Li, et al., “High-Safety Anode Materials for Advanced Lithium-Ion Batteries, Energy & Environmental,” *Materials* 7, no. 5 (2024): e12759.

5. M. Li, J. Lu, Z. Chen, and K. Amine, “30 Years of Lithium-Ion Batteries,” *Advanced Materials* 30, no. 33 (2018): e1800561.

6. S. K. Nemani, M. Torkamanzadeh, B. C. Wyatt, V. Presser, and B. Anasori, “Functional Two-Dimensional High-Entropy Materials,” *Communications Materials* 4, no. 1 (2023): 16.

7. B. Jin, G. Gao, Q. Zhao, et al., “Recycling Acidic Iron Wastewater for the Production of an Iron Oxalate Anode Material With Superior Long-Cycling Lithium Storage Ability,” *Journal of Materials Chemistry C* 13, no. 19 (2025): 9554–9567.

8. J. S. Yeoh, I. Di Bernardo, N. G. White, V. Otieno-Alego, T. Tsuzuki, and A. Lowe, “Iron-Based Energy Storage Materials From Carbon Dioxide and Scrap Metal,” *Materials Advances* 2, no. 1 (2021): 292–302.

9. B. Simon, S. Flandrois, K. Guerin, A. Fevrier-Bouvier, I. Teulat, and P. Biensan, “On the Choice of Graphite for Lithium Ion Batteries,” *Journal of Power Sources* 81–82 (1999): 312–316.

10. U. Kasavajjula, C. Wang, and A. J. Appleby, “Nano- and Bulk-Silicon-Based Insertion Anodes for Lithium-Ion Secondary Cells,” *Journal of Power Sources* 163, no. 2 (2007): 1003–1039.

11. M. C. López, J. L. Tirado, and C. Pérez Vicente, “Structural and Comparative Electrochemical Study of M(II) Oxalates, M = Mn, Fe, Co, Ni, Cu, Zn,” *Journal of Power Sources* 227 (2013): 65–71.

12. K. Zhang, Y. Li, Y. Wang, et al., “Enhanced Electrochemical Properties of Iron Oxalate With More Stable Li^+ Ions Diffusion Channels by Controlling Polymorphic Structure,” *Chemical Engineering Journal* 384 (2020): 123281.

13. Y. N. Zhang, S. S. Li, H. X. Kuai, et al., “Proton Solvent-Controllable Synthesis of Manganese Oxalate Anode Material for Lithium-Ion Batteries,” *RSC Advances* 11, no. 38 (2021): 23259–23269.

14. W. A. Ang, Y. L. Cheah, C. L. Wong, R. Prasanth, H. H. Hng, and S. Madhavi, “Mesoporous Cobalt Oxalate Nanostructures as High-Performance Anode Materials for Lithium-Ion Batteries: Ex Situ Electrochemical Mechanistic Study,” *Journal of Physical Chemistry C* 117, no. 32 (2013): 16316–16325.

15. J. Xu, L. He, H. Liu, et al., “Controlled Synthesis of Porous Anhydrous Cobalt Oxalate Nanorods With High Reversible Capacity and Excellent Cycling Stability,” *Electrochimica Acta* 170 (2015): 85–91.

16. K. Zhang, Y. Li, X. Hu, et al., “Inhibitive Role of Crystal Water on Lithium Storage for Multilayer $FeC_2O_4 \cdot xH_2O$ Anode Materials,” *Chemical Engineering Journal* 404 (2021): 126464.

17. B. Sun, L. Kuang, G. Li, et al., “Synergistic Structure and Oxygen-Vacancies Engineering of Lithium Vanadate for Kinetically Accelerated and Pseudocapacitance-Dominated Lithium Storage,” *Chemical Engineering Journal* 484 (2024): 149609.

18. J. Zhang, X. Bo, R. Wu, et al., “Transition Metal Carbonates/Oxalates for Advanced Lithium Storage: Optimization Strategies, further Faradic Reactions and Capacitive/Interfacial Charge Storage,” *Nano Energy* 139 (2025): 110928.

19. S. Liang, H. Wang, Y. Li, H. Qin, Z. Luo, and L. Chen, “Ternary Synergistic Transition Metal Oxalate 2D Porous Thin Sheets Assembled by 3D Nanoflake Array With High Performance for Supercapattery,” *Applied Surface Science* 567 (2021): 150809.

20. T. Chen, Z. Liu, H. Fan, L. Guo, and X. Tao, “Optimization Design of Orthorhombic-Monoclinic $Co_{1\text{-}x}Ni_xC_2O_4 \cdot 2H_2O$ Solid Solutions for High-Performance Pseudocapacitors,” *Journal of Alloys and Compounds* 808 (2019): 151722.

21. B. León, C. P. Vicente, and J. L. Tirado, “New Mixed Transition Metal Oxysalts as Negative Electrode Materials for Lithium-Ion Batteries,” *Solid State Ionics* 225 (2012): 518–521.

22. W. A. E. Ang, Y. L. Cheah, C. L. Wong, H. H. Hng, and S. Madhavi, “One-Pot Solvothermal Synthesis of $Co_{1\text{-}x}Mn_xC_2O_4$ and Their Application as Anode Materials for Lithium-Ion Batteries,” *Journal of Alloys and Compounds* 638 (2015): 324–333.

23. L. Wang, J. L. Shi, H. Su, et al., “Composite-Structure Material Design for High-Energy Lithium Storage,” *Small* 14, no. 34 (2018): e1800887.

24. Z. Liu, Y. Bai, H. Sun, et al., “Synergistic Dual-Phase Air Electrode Enables High and Durable Performance of Reversible Proton Ceramic Electrochemical Cells,” *Nature Communications* 15, no. 1 (2024): 472.

25. J. Wang, W. Bai, Y. Zhou, et al., “Sea Cucumber-Inspired Multi-Phase Metal Sulfides With Hierarchical Structure Towards Energy Storage With Promoted Safety,” *Journal of Energy Storage* 76 (2024): 109743.

26. Y. Zhou, Y. Wang, Y. Zhang, et al., “Abundant $Cu_3P/Co_2P/CoP$@NC Heterostructures Boost Charge Transfer Toward Fast and Durable Sodium Storage,” *Carbon Energy* 7, no. 6 (2025): e721.

27. A. Lichchhavi, A. Kanwade, and P. M. Shirage, “A Review on Synergy of Transition Metal Oxide Nanostructured Materials: Effective and Coherent Choice for Supercapacitor Electrodes,” *Journal of Energy Storage* 55 (2022): 105692.

28. H. M. Rietveld, “Line Profiles of Neutron Powder-Diffraction Peaks for Structure Refinement,” *Acta Crystallographica* 22, no. 1 (1967): 151–152.

29. H. M. Rietveld, “A Profile Refinement Method for Nuclear and Magnetic Structures,” *Journal of Applied Crystallography* 2, no. 2 (1969): 65–71.

30. B. Krüner, A. Schreiber, A. Tolosa, et al., “Nitrogen-Containing Novolac-Derived Carbon Beads as Electrode Material for Supercapacitors,” *Carbon* 132 (2018): 220–231.

31. M. Zeiger, N. Jäckel, D. Weingarth, and V. Presser, “Vacuum or Flowing Argon: What Is the Best Synthesis Atmosphere for Nanodiamond-Derived Carbon Onions for Supercapacitor Electrodes?,” *Carbon* 94 (2015): 507–517.

32. T. Marino, M. Toscano, N. Russo, and A. Grand, “Structural and Electronic Characterization of the Complexes Obtained by the Interaction Between Bare and Hydrated First-Row Transition-Metal Ions (Mn^{2+}, Fe^{2+}, Co^{2+}, Ni^{2+}, Cu^{2+}, Zn^{2+}) and Glycine,” *Journal of Physical Chemistry B* 110, no. 48 (2006): 24666–24673.

33. A. M. Mohammed, “Hydration Structure and Water Exchange Dynamics of Fe(II) Ion in Aqueous Solution,” *Bulletin of the Chemical Society of Ethiopia* 24, no. 2 (2010): 239–250.

34. C. Zhao, Y. Jiang, S. Liang, F. Gao, L. Xie, and L. Chen, “Two-Dimensional Porous Nickel Oxalate Thin Sheets Constructed by Ultrathin Nanosheets as Electrode Materials for High-Performance Aqueous Supercapacitors,” *CrystEngComm* 22, no. 17 (2020): 2953–2963.

35. I. Persson, “Hydrated Metal Ions in Aqueous Solution: How Regular Are Their Structures?,” *Pure and Applied Chemistry* 82, no. 10 (2010): 1901–1917.

36. J. Kopp, P. Novák, S. Lisníková, V. Vrba, and V. Procházka, “Co-Precipitation of Fe-Cu Bimetal Oxalates in An Aqueous Solution and Their Thermally Induced Decomposition,” *European Journal of Inorganic Chemistry* 2021, no. 37 (2021): 3886–3895.

37. S. Caric, “Amélioration de la Structure de la Humboldtine $FeC_2O_4 \cdot 2H_2O$,” *Bulletin of the French Society of Mineralogy and Crystallography* 82 (1959): 50–55.

38. L. Zwiener, F. Girgsdies, R. Schlögl, and E. Frei, “Investigations of Cu/Zn Oxalates From Aqueous Solution: Single-Phase Precursors and Beyond,” *Chemistry – A European Journal* 24, no. 56 (2018): 15080–15088.

39. A. N. Christensen, B. Lebech, N. H. Andersen, and J.-C. Grivel, “The Crystal Structure of Paramagnetic Copper(II) Oxalate (CuC_2O_4): Formation and Thermal Decomposition of Randomly Stacked Anisotropic Nano-Sized Crystallites,” *Dalton Transactions* 43, no. 44 (2014): 16754–16768.

40. A. Koleżyński, B. Handke, and E. Drożdż-Cieśla, “Crystal Structure, Electronic Structure, and Bonding Properties of Anhydrous Nickel Oxalate,” *Journal of Thermal Analysis and Calorimetry* 113, no. 1 (2013): 319–328.

41. J. Romann, V. Chevallier, A. Merlen, and J.-C. Valmalette, “Self-Organized Assembly of Copper Oxalate Nanocrystals,” *Journal of Physical Chemistry C* 113, no. 13 (2009): 5068–5074.

42. M. C. D'Antonio, A. Wladimirsky, D. Palacios, et al., “Spectroscopic Investigations of Iron(II) and Iron(III) Oxalates,” *Journal of the Brazilian Chemical Society* 20, no. 3 (2009): 445–450.

43. W. Song, J. Zhang, C. Wen, et al., “Synchronous Redox Reactions in Copper Oxalate Enable High-Capacity Anode for Proton Battery,” *Journal of the American Chemical Society* 146, no. 7 (2024): 4762–4770.

44. I. I. Conde-Morales, L. Hinojosa-Reyes, J. L. Guzmán-Mar, and A. Hernández-Ramírez, “I.D.C. Sáenz-Tavera, M. Villanueva-Rodríguez, Different Iron Oxalate Sources as Catalysts on Pyrazinamide Degradation by the Photo-Fenton Process at Different pH Values,” *Water, Air, & Soil Pollution* 231, no. 8 (2020): 425.

45. K. Chen, Z. Li, K. Zhang, et al., “Coordinate Regulation of Amorphous Carbon Microspheres and Crystal Structure of Iron Oxalate for High Rate Lithium Storage Ability,” *Journal of Alloys and Compounds* 1008 (2024): 176844.

46. Y. Zhang, C. Wang, Y. Dong, R. Wei, and J. Zhang, “Understanding the High-Performance Anode Material of $CoC_2O_4 \cdot 2H_2O$ Microrods Wrapped by Reduced Graphene Oxide for Lithium-Ion and Sodium-Ion Batteries,” *Chemistry – A European Journal* 27, no. 3 (2021): 993–1001.

47. L. Wang, R. Zhang, Y. Jiang, et al., “Interfacial Synthesis of Micro-Cuboid $Ni_{0.55}Co_{0.45}C_2O_4$ Solid Solution With Enhanced Electrochemical Performance for Hybrid Supercapacitors,” *Nanoscale* 11, no. 29 (2019): 13894–13902.

48. X. L. Wang, E. M. Jin, G. Sahoo, and S. M. Jeong, “High-Entropy Metal Oxide $(NiMnCrCoFe)_3O_4$ Anode Materials With Controlled Morphology for High-Performance Lithium-Ion Batteries,” *Batteries* 9, no. 3 (2023): 147.

49. B. Shen, Z. Chen, H. Mao, et al., “CTAB-Induced Synthesis of Two-Dimensional Copper Oxalate Particles: Using L-Ascorbic Acid as the Source of Oxalate Ligand,” *RSC Advances* 14, no. 32 (2024): 23225–23231.

50. F.-F. Xing, X.-Y. Huang, Y.-X. He, et al., “Synthesis of Mesoporous Rod-Like MnC_2O_4/MWCNT Composite Anode Material for Lithium-Ion Batteries,” *Journal of Electronic Materials* 52, no. 6 (2023): 4179–4190.

51. S. Chenakin and N. Kruse, “XPS Characterization of Transition Metal Oxalates,” *Applied Surface Science* 515 (2020): 146041.

52. K. Zhang, Q. Zhao, D. Cui, et al., “Enhancing Electrochemical Lithium-Storage Properties of Hydrated Iron Oxalate ($FeC_2O_4 \cdot 2H_2O$) Anode Material by Combining With Dual-States Copper,” *Journal of Alloys and Compounds* 976 (2024): 173036.

53. Z. Li, Q. Zhao, K. Zhang, et al., “Achieving Super Lithium Storage of FeC_2O_4/Gs Composites With Dual-Level Structured Graphene Sheets Through Electrostatic Adherence,” *Journal of Materials Chemistry C* 12, no. 37 (2024): 15012–15023.

54. S. Chenakin and N. Kruse, “Thermal Decomposition of Nickel Oxalate Dihydrate: A Detailed XPS Insight,” *Journal of Physical Chemistry C* 123, no. 51 (2019): 30926–30936.

55. S. P. Chenakin, R. Szukiewicz, R. Barbosa, and N. Kruse, “Surface Analysis of Transition Metal Oxalates: Damage Aspects,” *Journal of Electron Spectroscopy and Related Phenomena* 209 (2016): 66–77.

56. S. P. Chenakin and N. Kruse, “Surface Composition and Electronic Properties of Co-Cu Mixed Oxalates: A Detailed XPS Analysis,” *Applied Surface Science* 669 (2024): 160460.

57. K. Zhang, D. Cui, X. Huang, et al., “Insights into the Interfacial Chemistry and Conversion Mechanism of Iron Oxalate Toward the Reduction by Lithium,” *Chemical Engineering Journal* 426 (2021): 131446.

58. Y. Jia, A. Cheng, W. Ke, et al., “Hierarchical Structure Constructed by Manganese Oxalate Framework With Accurate Iron Doping for Ultra-Efficient Lithium Storage,” *Electrochimica Acta* 380 (2021): 138217.

59. F. Feng, W. Kang, F. Yu, H. Zhang, and Q. Shen, “High-Rate Lithium Storage Capability of Cupric-Cobaltous Oxalate Induced by Unavoidable Crystal Water and Functionalized Graphene Oxide,” *Journal of Power Sources* 282 (2015): 109–117.

60. W. Kang and Q. Shen, “The Shape-Controlled Synthesis and Novel Lithium Storage Mechanism of as-Prepared $CuC_2O_4 \cdot xH_2O$ Nanostructures,” *Journal of Power Sources* 238 (2013): 203–209.

61. M. J. Aragón, B. León, T. Serrano, C. Pérez Vicente, and J. L. Tirado, “Synergistic Effects of Transition Metal Substitution in Conversion Electrodes for Lithium-Ion Batteries,” *Journal of Materials Chemistry* 21, no. 27 (2011): 10102.

62. Y. Zhang, Z. Lu, M. Guo, Z. Bai, and B. Tang, “Porous CoC_2O_4 Nanorods as High Performance Anode Material for Lithium Ion Batteries,” *JOM* 68, no. 11 (2016): 2952–2957.

63. X. Yang, H. Wang, Y. Song, et al., "Low-Temperature Synthesis of a Porous High-Entropy Transition-Metal Oxide as an Anode for High-Performance Lithium-Ion Batteries," *ACS Applied Materials & Interfaces* 14, no. 23 (2022): 26873–26881.

64. T. C. Liu, W. G. Pell, B. E. Conway, and S. L. Roberson, "Behavior of Molybdenum Nitrides as Materials for Electrochemical Capacitors: Comparison With Ruthenium Oxide," *Journal of the Electrochemical Society* 145, no. 6 (1998): 1882–1888.

65. J. Wang, J. Polleux, J. Lim, and B. Dunn, "Pseudocapacitive Contributions to Electrochemical Energy Storage in TiO_2 (Anatase) Nanoparticles," *Journal of Physical Chemistry C* 111, no. 40 (2007): 14925–14931.

66. E. W. C. Spotte-Smith, R. L. Kam, D. Barter, et al., "Toward a Mechanistic Model of Solid-Electrolyte Interphase Formation and Evolution in Lithium-Ion Batteries," *ACS Energy Letters* 7, no. 4 (2022): 1446–1453.

67. M. H. Hossain, M. A. Chowdhury, N. Hossain, M. A. Islam, and M. H. Mobarak, "Advances of Lithium-Ion Batteries Anode Materials—A Review," *Chemical Engineering Journal Advances* 16 (2023): 100569.

68. F. Baakes, D. Witt, and U. Krewer, "Impact of Electrolyte Impurities and SEI Composition on Battery Safety," *Chemical Science* 14, no. 47 (2023): 13783–13798.

69. C. Hu, M. Geng, H. Yang, et al., "A Review of Capacity Fade Mechanism and Promotion Strategies for Lithium Iron Phosphate Batteries," *Coatings* 14, no. 7 (2024): 832.

70. K. Zhang, R. Xu, R. Wei, et al., "Tunable Polymorph and Morphology Synthesis of Iron Oxalate Nanoparticles as Anode Materials for Lithium Ion Batteries," *Materials Chemistry and Physics* 243 (2020): 122676.

71. C. Heubner, K. Nikolowski, S. Reuber, M. Schneider, M. Wolter, and A. Michaelis, "Recent Insights into Rate Performance Limitations of Li-Ion," *Batteries, Batteries & Supercaps* 4, no. 2 (2020): 268–285.

72. K. Zhang, D. Zhang, Y. Li, et al., "$FeC_2O_4@Fe_2O_3$/rGO Composites With a Novel Interfacial Characteristic and Enhanced Ultrastable Lithium Storage Performance," *Applied Surface Science* 507 (2020): 145051.

73. W. A. Ang, N. Gupta, R. Prasanth, and S. Madhavi, "High-Performing Mesoporous Iron Oxalate Anodes for Lithium-Ion Batteries," *ACS Applied Materials & Interfaces* 4, no. 12 (2012): 7011–7019.

74. T. Song, G. Gao, D. Cui, et al., "Achieving Ultrastability and Efficient Lithium Storage Capacity With High-Energy Iron(II) Oxalate Anode Materials by Compositing Ge Nano-Conductive Sites," *Nanoscale* 15, no. 6 (2023): 2700–2713.

75. Y. Zhang, Y. Dong, R. Wei, et al., "Rod-Like $Ni_{0.5}Co_{0.5}C_2O_4.2H_2O$ In-Situ Formed on rGO by an Interface Induced Engineering: Extraordinary Rate and Cycle Performance as an Anode in Lithium-Ion and Sodium-Ion Half/Full Cells," *Journal of Colloid and Interface Science* 607, no. Pt 2 (2022): 1153–1162.

76. Y. Lu, X. Hou, L. Miao, et al., "Cyclohexanehexone With Ultrahigh Capacity as Cathode Materials for Lithium-Ion Batteries," *Angewandte Chemie International Edition* 58, no. 21 (2019): 7020–7024.

77. Y. Zhao, X. Li, B. Yan, et al., "Recent Developments and Understanding of Novel Mixed Transition-Metal Oxides as Anodes in Lithium Ion Batteries," *Advanced Energy Materials* 6, no. 8 (2016): 1502175.

78. B. Ran, R. Cheng, Y. Zhong, et al., "High Entropy Activated and Stabilized Nickel-Based Prussian Blue Analogue for High-Performance Aqueous Sodium-Ion Batteries," *Energy Storage Materials* 71 (2024): 103583.

79. Y. Liu, T. Liu, X. Wang, et al., "Subsurface Electron Trap Enabled Long-Cycling Oxalate-Based Li-CO_2 Battery," *Advanced Materials* 37, no. 39 (2025): e2507871.

80. B. S. Parimalam, A. D. MacIntosh, R. Kadam, and B. L. Lucht, "Decomposition Reactions of Anode Solid Electrolyte Interphase (SEI) Components With $LiPF_6$," *Journal of Physical Chemistry C* 121, no. 41 (2017): 22733–22738.

81. M. Dixit, B. Witherspoon, N. Muralidharan, et al., "Insights into the Critical Materials Supply Chain of the Battery Market for Enhanced Energy Security," *ACS Energy Letters* 9, no. 8 (2024): 3780–3789.

82. Y. Zhang, H. Shen, Y. Li, Y. Hu, and Y. Li, "Prelithiation Strategies for Enhancing the Performance of Lithium-Ion Batteries," *RSC Advances* 15, no. 2 (2025): 1249–1274.

83. Z. Li, J. Jin, Z. Yuan, and W. Yang, "Surface Modification of SiOx Film Anodes by Laser Annealing and Improvement of Cyclability for Lithium-Ion Batteries," *Materials Science in Semiconductor Processing* 121 (2021): 105300.

Supporting Information

Additional supporting information can be found online in the Supporting Information section.

The supporting information mainly includes the following: Refined lattice parameters for the TMOx 0-2 from powder X-ray diffraction data; Energy dispersive spectroscopy elemental analysis results of TMOx-3; Elemental EDS mapping of TMOx-0 and TMOx-1; EIS fitting parameters of all TMOx electrodes for fresh cells and after 100 cycles at the rate of 100 mA/g; CV curves and their kinetic analysis at different scan rates (0.2-2 mV/s); X-ray diffractograms, Raman spectra, and thermogravimetric and differential thermogravimetric data of TMOx-3; Contents of five transition metal elements in multi-phase transition metal oxalates obtained by inductively coupled plasma-optical emission spectroscopy; The digital photos of all samples; High-resolution X-ray photoelectron spectra of TMOx-0, TMOx-1, and TMOx-3; Scanning electron micrographs of the electrodes before and after cycling; X-ray diffractograms of TMOx 0-2 electrodes before and after cycling; Electrochemical characterization of single transition metal oxalates.